MATERIALS SCIENCE

# Enabling an ultraefficient lithium-selective construction through electric field–assisted ion control

**Yan Zhao[1,2]*†, Xue Yan[3]†, Lei Xia[4]*, Yangbo Qiu[2], Shuang Zheng[2], Gang Lu[2]§, Yaoming Wang[5], Yang Zhang[6], Jiangnan Shen[7], Xi Zhang[8], Xing Yang[1]*, Jefferson Zhe Liu[2], Raf Dewil[8,9], Congjie Gao[7], Bart Van der Bruggen[1]***

Copyright © 2025 The Authors, some rights reserved; exclusive licensee American Association for the Advancement of Science. No claim to original U.S. Government Works. Distributed under a Creative Commons Attribution NonCommercial License 4.0 (CC BY-NC).

**Membranes with precise ion transport behaviors are regarded as an alternative for lithium (Li) extraction from water streams. Current membranes demonstrate limited viability due to the lack of efficient $Li^+$-selective architectures. We propose an electric field–assisted ion control hypothesis in reinforcing ultraefficient $Li^+$-selective membranes, in which an ionized zeolitic imidazolate framework layer (Q-PEI@ZIF) is constructed via polyethylenimine (PEI) in situ confinement conversion and subsequent quaternization of 2,3-epoxypropyl trimethyl ammonium chloride. In electrodialysis at 5 milliampere per square centimeter, the resulting membrane Q(5%)-PEI(1.0)@ZIF#CEM shows that the ion permeation rates follow the order of $K^+ \sim Li^+ > Na^+ > Ca^{2+} \sim Mg^{2+}$, corresponding to 0.31, 0.30, 0.25, 0, and 0 mole per square meter per hour in 120 minutes, respectively. With a 25-millimolar $Li^+$/$Mg^{2+}$ mixed solution, it exhibits an unprecedented $Li^+/Mg^{2+}$ permselectivity of 20,000 and 99.99% purity of $Li^+$ product in 120 minutes. This study expands the hypothesis of electric field–assisted ion control in enabling an ultraefficient $Li^+$-selective construction.**

## INTRODUCTION

Lithium ($Li^+$) recovery from water streams is a sustainable method for overcoming Li shortages and reducing the environmental impacts of exploitation from mineral ores (*1*). Membrane technologies, recognized for their efficient, low-energy, and scalable separation processes, have been extensively explored in harvesting ion resources from water streams (*2*–*4*). Among these, electrodialysis and nanofiltration are two of the most prominent methods for ion separation. In particular, electro-driven membranes, equipped with ion exchange capacity and the ability to mitigate challenges such as high-concentration gradients and osmotic pressure (which commonly affect nanofiltration membranes), have been increasingly developed and integrated into electrochemical systems for ion separation (*5*, *6*). To enable ion recovery from water streams, research efforts are focused on constructing membranes with high-target ion selectivity. These membranes are prepared mainly via controlling membrane structures (e.g., pore size sieving) or functional groups (e.g., surface electrostatic repulsion and binding affinity) to exploit the interaction between hydrated ions and membranes (*7*). For example, membrane modification with positively charged layers on the surface (*8*, *9*), construction of a membrane structure with controllable pore size (*10*), or fabrication of the membrane materials with high binding affinity groups (*11*), have been used to improve monovalent cation selectivity. However, current membranes still suffer from an extremely low efficiency in separating $Li^+$ from other coexisting ions, such as the similar cations of $Mg^{2+}$ and $Na^+$ (*12*, *13*). In addition, these ion-selective mechanisms tend to impede ion throughput, resulting in a low $Li^+$ permeation rate and thus the permeability-selectivity trade-offs (*14*, *15*).

With nanometer-sized pores and a powerful capacity for multifunctional construction, metal-organic frameworks (MOFs) open an avenue for ion-selective transport. Recent studies have explored them to be an ideal material that allows $Li^+$ transport while rejecting other mixed cations in electro-driven processes (*16*–*18*). Nevertheless, it is limited in the separation of ions with similar hydration radius if only based on size sieving effects of MOFs (*19*). Besides, it is technically challenging to fabricate defect-free and stable MOF layers on a membrane surface (*20*). In addition, because of the Gibbs-Donnan effect, the insufficiency of ion exchange sites in MOFs leads to slow ion transport (*21*). Furthermore, ion transport through the non-charged cavities of MOFs may cause hydrolysis issues (*22*). Thus far, MOF-based membranes have had limited success in effective ion selectivity in electro-driven systems.

Recently, hybrid MOF-based composite membranes that combine the easy processing of functional polymers and tunable pores of MOFs have been explored to equip them with well-defined crystal structures and coordination functional groups (*23*–*25*). To some extent, MOFs can be constructed on the membrane surface via an in situ growth method. However, this structure is typically thick and easily disintegrates because of the stacking of the crystals (*18*), thereby largely limiting the ion permeation rate while suffering from stability issues (*26*). In our recent work, a zeolitic imidazolate framework (ZIF)–based anion exchange membrane with monovalent anion selectivity was facilely fabricated by coating a polydopamine on ZIFs under an alternating current electric field (*27*).

Theoretically, ion species exhibit unique ionic charge density and corresponding ion hydration shells, resulting in specific interactions with surrounding molecules/materials (*7*). Under an electric field,

[1]Department of Chemical Engineering, KU Leuven, Celestijnenlaan 200F, B-3001 Leuven, Belgium. [2]Department of Civil Engineering, The University of Hong Kong, Hong Kong 999077, China. [3]Department of Mechanical Engineering, The University of Melbourne, Parkville, VIC 3010, Australia. [4]Division of Soil and Water Management, KU Leuven, Kasteelpark Arenberg 20, B-3001 Leuven, Belgium. [5]Key Laboratory of Precision and Intelligent Chemistry, Department of Applied Chemistry, School of Chemistry and Material Science, University of Science and Technology of China, Hefei, P. R. China. [6]College of Environment and Safety Engineering, Qingdao University of Science and Technology, Qingdao 266042, China. [7]College of Chemical Engineering, Zhejiang University of Technology, Hangzhou 310014, China. [8]Department of Chemical Engineering, KU Leuven, Process and Environmental Technology Lab, J. De Nayerlaan 5, B-2860 Sint-Katelijne-Waver, Belgium. [9]Department of Engineering Science, University of Oxford, Parks Road, Oxford OX1 3PJ, UK.
*Corresponding author. Email: yan.zhao@kuleuven.be (Y.Z.); lei.xia@kuleuven.be (L.X.); xing.yang@kuleuven.be (X. Yang); bart.vanderbruggen@kuleuven.be (B.V.d.B.)
†These authors contributed equally to this work.
§Present address: Department of Chemical and Biomolecular Engineering, University of Pennsylvania, Philadelphia, PA 19104, USA.

these ions gain kinetic energy, enabling precise control via an external electric field (*5*, *28*). Inspired by biological cell membranes, where ion channels enable rapid and selective transport via tunable charge density, geometric filtering (pore size and charge compatibility) (*29*–*32*), herein, we design a class of composite MOF membrane via the in situ growth of ZIFs threaded with linear polyethylenimine (PEI) onto a commercial cation exchange membrane (CEM) substrate (Fig. 1A). This prepared PEI@ZIF#CEM has ample -$NH_2$ groups and is further reacted with the 2,3-epoxypropyl trimethyl ammonium chloride (ETAC) monomer (with quaternary ammonium group) through an alternating current electric field–assisted $Li^+$ control assembly process (*28*, *33*) to construct the Q-PEI@ZIF#CEM (figs. S1 to S5). A catalyst, tris(dimethylaminomethyl)phenol (DMP-30), is used to accelerate the epoxy groups (in ETAC) reacting with amino groups (in PEI@ZIF). To investigate the effect of PEI and ETAC contents on the resulting membranes, the Q-PEI@ZIF#CEM membranes are prepared with varying PEI content of 0, 0.5, 1.0, and 2.0 g $liter^{-1}$ (in the construction of the PEI@ZIF architecture process), and different ETAC content of 0, 5, and 10 wt % (in LiCl assembly process). This bioinspired design merges stimuli-responsive regulation with Q-PEI@ZIF structural precision and achieves ultra-efficient ion selectivity via advancing separation systems. These membranes are denoted as pristine CEM, ZIF#CEM, Q(5%)-ZIF#CEM, PEI(1.0)@ZIF#CEM, Q(5%)-PEI(0.5)@ZIF#CEM, Q(5%)-PEI(1.0)@ZIF#CEM, Q(5%)-PEI(2.0)@ZIF#CEM, and Q(10%)-PEI(1.0)@ZIF#CEM, respectively (table S2).

## RESULTS

Figure 1B shows the cross-sectional scanning electron microscopy (SEM) images of a pristine CEM [Fig. 1B (i)] and Q(5%)-PEI(1.0)@ZIF#CEM [Fig. 1B (ii)], and a uniformly distributed layer (~4 μm thick) can be observed on the pristine CEM membrane surface (fig. S6). Attenuated total refraction–Fourier transform infrared spectroscopy spectra (ATR-FTIR; fig. S7) of these crystals indicate that secondary amine group characteristic peaks of 1567, 1418, and 954 $cm^{-1}$ exist in both ZIF#CEM and Q(5%)-PEI(1.0)@ZIF#CEM, mainly due to the C—N groups in the 2-methylimidazole (*34*). To further analyze these chemical components, x-ray photoelectron spectroscopy (XPS) of ZIFs and Q(5%)-PEI(1.0)@ZIF and their high-resolution (C 1s, N 1s, and O 1s) are used to illustrate the element contents (atomic%) and existing chemical bonds, respectively (Fig. 1C). Compared to the pure ZIFs, the elements of O 1s and N 1s in Q(5%)-PEI(1.0)@ZIF increased from 7.7 to 9.7% and from 16.1 to 18.2%, respectively, due to the ETAC monomer introduced into Q(5%)-PEI(1.0)@ZIF. The bonds of C—O (287.4 eV) and $C—N^+$ (286.1 eV) appearing in the Q(5%)-PEI(1.0)@ZIF confirm that the increased amount of O and N may come from -C—OH and -$C—N^+R_3$ in the structure, which

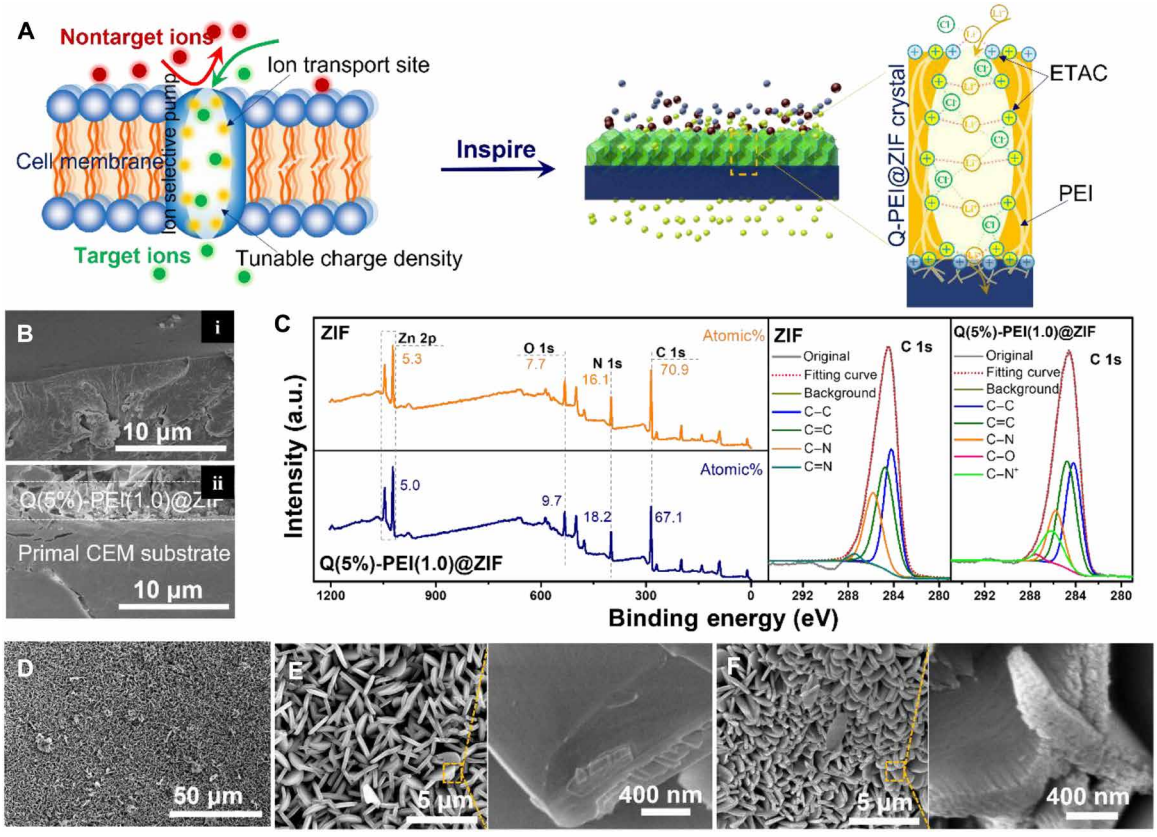



**Fig. 1. Q(5%)-PEI(1.0)@ZIF#CEM preparation and characterization.** (**A**) The target ion selectivity channel in the biological cell membrane inspired us to design numerous Q-PEI@ZIF crystals for $Li^+$ selectivity. (**B**) Cross-sectional SEM images of the CEM (i) and the Q(5%)-PEI(1.0)@ZIF#CEM (ii). (**C**) XPS of the surface elements (atomic %) of ZIFs and Q(5%)-PEI(1.0)@ZIF and their C 1s high-resolution images. (**D**) The homogeneous, intergrown, and continuous Q(5%)-PEI(1.0)@ZIF#CEM surface SEM image. The morphology of ZIF (**E**) and Q(5%)-PEI(1.0)@ZIF (**F**) crystals is observed by the SEM images.

may be generated by the substitution reaction between -$NH_2$ (in PEI(1.0)@ZIF) and epoxy group in ETAC (figs. S8 and S9). Figure 1D shows a homogeneous, intergrown, and continuous Q(5%)-PEI(1.0)@ZIF layer. The pure ZIF crystals with the homogeneous and hollow framework and the vacancies between ZIF crystals can be observed on the CEM surface (Fig. 1E). When in situ confinement conversion of PEI and alternating current electrical field–assisted $Li^+$ control in assembling of ETAC is applied, the Q(5%)-PEI(1.0)@ZIF shows a much rougher crystal (Fig. 1F), which reflects the changed morphology of the crystal on the membrane surface.

Figure 2A shows a large area (a 6.0-cm diameter) of Q(5%)-PEI(1.0)@ZIF layer constructed on the CEM surface. The roughness of this layer is characterized by atomic force microscopy (AFM), showing a maximum height of ~1.7 μm (Fig. 2B). It reflects an increase of membrane-specific surface area and a uniform distribution of a defect-free Q(5%)-PEI(1.0)@ZIF layer. The increased roughness of the Q(5%)-PEI(1.0)@ZIF crystal is observed by the amplification of AFM images compared to that of the pure ZIF crystal (fig. S10). The x-ray diffraction (XRD) patterns of the ZIF and PEI@ZIF crystals are presented in Fig. 2C. Subtle shifts in the characteristic peaks of PEI@ZIF are observed compared to those of the unmodified ZIF, which can be attributed to the incorporation of the PEI polymer within the ZIF framework. Similarly, when the Q(5%)-PEI(1.0)@ZIF composite is fabricated on the pristine CEM membrane [Q(5%)-PEI(1.0)@ZIF#CEM], the XRD pattern (Fig. 2D) retains the distinctive ZIF-derived peaks but exhibits minor shifts relative to the pristine ZIF#CEM. The threaded PEI polymer in ZIF followed by ETAC quaternization, may shift the pore size of the ZIF in Q(5%)-PEI(1.0)@ZIF#CEM and form a cushion-shaped cavity, which is expected to be 0.94 by 0.70 by 0.54 nm (*35*). A nitrogen ($N_2$) adsorption isotherm at 77 K is measured to determine the porous structure (*36*). Compared to the ZIFs, the Brunauer-Emmett-Teller (BET) surface area of the Q(5%)-PEI(1.0)@ZIF increases from 3.0 to 5.8 $m^2 \cdot g^{-1}$ (Fig. 2E). It suggests the enhanced access of $N_2$ molecules within

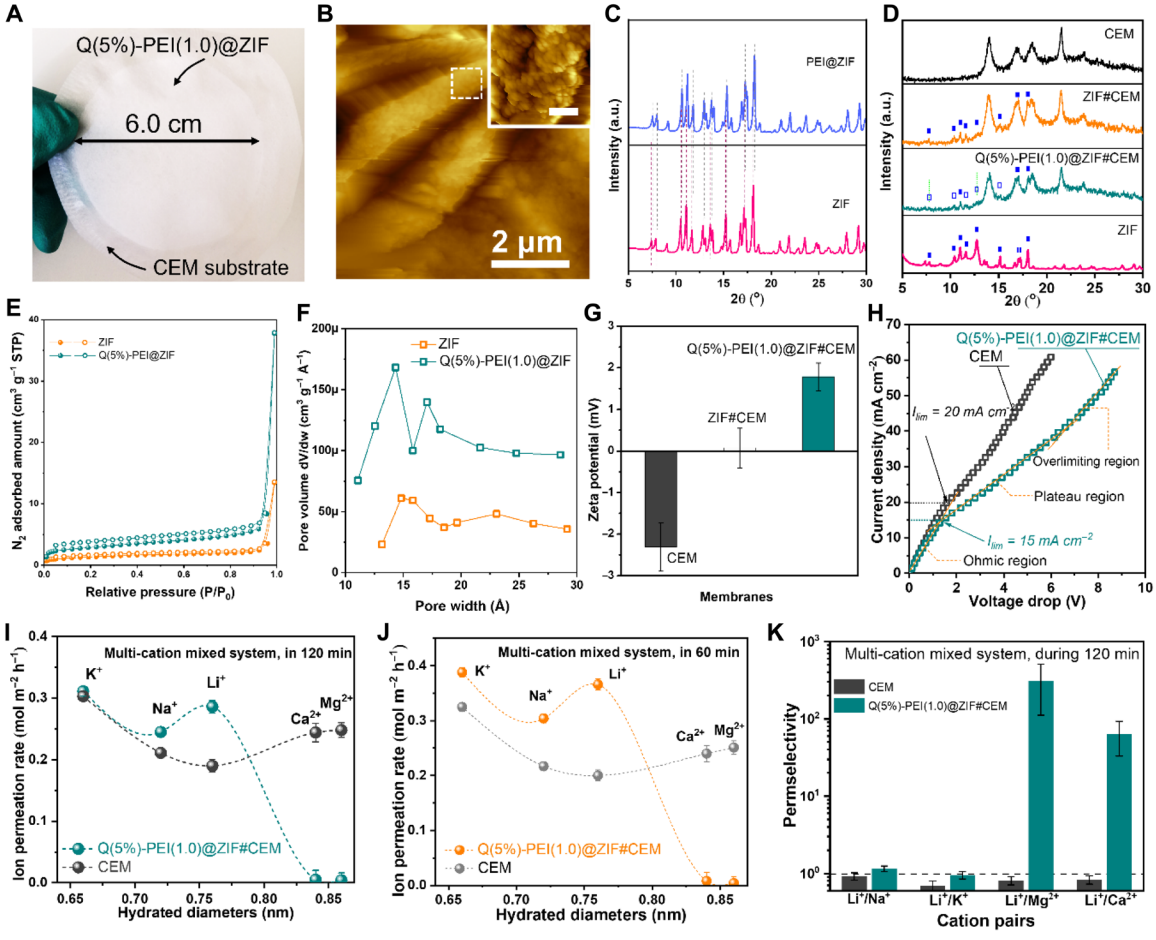



**Fig. 2. Membrane surface characteristics and ion transport behaviors.** (**A**) Photograph of the commercial CEM and the fabricated Q(5%)-PEI(1.0)@ZIF layer on the surface. (**B**) AFM topographic image of the Q(5%)-PEI(1.0)@ZIF on CEM. Scale bar (zoomed-in AFM images), 100 nm. XRD patterns of (**C**) ZIF and PEI@ZIF crystals, and (**D**) CEM, ZIF#CEM and Q(5%)-PEI(1.0)@ZIF#CEM. (**E**) BET adsorption isotherms, measured at standard temperature and pressure (STP, 273 K and 101.325 kPa), of ZIF and Q(5%)-PEI(1.0)@ZIF with $N_2$. (**F**) Pore size distribution is derived from $N_2$ sorption by using the HK method. (**G**) Approximations of CEM, ZIF#CEM, and Q(5%)-PEI(1.0)@ZIF#CEM surface charge by zeta potential via streaming potential measurements (pH 7). (**H**) Polarization current density-voltage behaviors of CEM and Q(5%)-PEI(1.0)@ZIF#CEM membranes. The ion permeation of cations through CEM and Q(5%)-PEI(1.0)@ZIF#CEM membranes in 120 min (**I**) and 60 min (**J**). Dashed lines are added as visual guides. (**K**) $Li^+/M^{z+}$ permselectivity ($M^{z+}$: $Na^+$, $K^+$, $Mg^{2+}$, and $Ca^{2+}$) through CEM and Q(5%)-PEI(1.0)@ZIF#CEM. Dashed lines are added as guides that membrane with (P > 1)/without (P < 1) $Li^+$ selectivity. h, hours. a.u., arbitrary unit.

the porous material in this Q(5%)-PEI(1.0)@ZIF and confirms the retention of ZIF microporosity. The pore size distribution derived from $N_2$ (3.40-Å kinetic diameter) sorption is calculated on the basis of the Horváth-Kawazoe (HK) method, showing smaller pores of the Q(5%)-PEI(1.0)@ZIF (14.6-Å pore width) than that of ZIF (16.8-Å pore width) (Fig. 2F). The zeta potentials of the membranes (Fig. 2G) are quantified to explore the influence of the electrostatic interaction of the membrane surface on the ion separation. In neutral conditions (pH 7), as shown in fig. S11, the negative charge (−2.4 mV) of the commercial CEM is due to the cation exchange groups in the membrane structure. The pure ZIF nanocrystals on the ZIF#CEM surface show an almost zero zeta potential, indicating the lack of charged groups in this layer. In contrast, a positive charge of +1.9 mV is determined for the Q(5%)-PEI(1.0)@ZIF#CEM, which is ascribed to the introduction of PEI and ETAC molecules with positive charges in the crystal layer. In addition, the positive charge effect is more pronounced in Q(5%)-PEI(1.0)@ZIF#CEM with a rougher surface, and thus, multivalent cations face stronger electrostatic repulsion when being transported through the membrane.

The electrochemical behavior of the membrane is measured in a 0.10 M NaCl solution in a laboratory-designed device (fig. S12). The surface electrical resistance of CEM is 3.02 ohm·cm$^2$, and all the prepared membranes show an increased surface electrical resistance (fig. S13). The surface electrical resistance of ZIF#CEM is as high as 13.50 ohm·cm$^2$ due to the lack of charged groups, indicating a high resistance for ion transport. However, intercalation of PEI in ZIF crystals and further quantization with ETAC can minimize the increased surface electrical resistance due to the increased surface charge density. Thus, the surface electrical resistance of Q(5%)-PEI(1.0)@ZIF is only increased by 1.8 ohm·cm$^2$ compared to the CEM. Figure 2H shows a 15 mA·cm$^{-2}$ limiting current density of the Q(5%)-PEI(1.0)@ZIF#CEM, which is lower than that of the CEM (i.e., 20 mA·cm$^{-2}$ limiting current density, fig. S14). The decreased limiting current density is caused by Q(5%)-PEI(1.0)@ZIF, and caution should be taken to choose the operating conditions of this resulting membrane under the limiting current density (Ohmic region) in electrodialysis.

Five cations ($Li^+$, $Na^+$, $K^+$, $Mg^{2+}$, and $Ca^{2+}$) commonly found in water streams are selected, and their permeation is measured in electrodialysis by using a cocktail solution. The ion permeation rate and the $Li^+/M^{z+}$ ($M^{z+}$: $Na^+$, $K^+$, $Mg^{2+}$, and $Ca^{2+}$) permselectivity are calculated to evaluate the transport behavior of different cations. In electrodialysis at a constant current density of 5 mA·cm$^{-2}$, all cations transport through the pristine CEM (the commercial cation exchange membrane) and accumulate in the concentrated chamber (fig. S15A). During the 120 min, the transport order of this pristine CEM is $K^+$ (0.31 mol m$^{-2}$·hour$^{-1}$) > $Ca^{2+}$ (0.25 mol m$^{-2}$·hour$^{-1}$) ~ $Mg^{2+}$ (0.25 mol m$^{-2}$·hour$^{-1}$) > $Na^+$ (0.22 mol m$^{-2}$·hour$^{-1}$) > $Li^+$ (0.18 mol m$^{-2}$·hour$^{-1}$) (Fig. 2I); while, the transport ability order about the Q(5%)-PEI(1.0)@ZIF#CEM is $K^+$ ~ $Li^+$ > $Na^+$, and the divalent cations ($Mg^{2+}$ and $Ca^{2+}$) are rejected (fig. S15B and Fig. 2I) during the 120 min. To decrease the effect of the polarization phenomenon caused by excessive running time in the electro-driven system, we also calculate the ion transport ability order through the pristine CEM and Q(5%)-PEI(1.0)@ZIF#CEM during the 60 min: The ion transport ability order through the pristine CEM is $K^+$ (0.34 mol m$^{-2}$·hour$^{-1}$) > $Ca^{2+}$ (0.26 mol m$^{-2}$·hour$^{-1}$) ~ $Mg^{2+}$ (0.26 mol m$^{-2}$·hour$^{-1}$) > $Na^+$ (0.23 mol m$^{-2}$·hour$^{-1}$) > $Li^+$ (0.19 mol m$^{-2}$·hour$^{-1}$), and through the Q(5%)-PEI(1.0)@ZIF#CEM is $K^+$ ~ $Li^+$ > $Na^+$ > > $Ca^{2+}$ (0 mol m$^{-2}$·hour$^{-1}$) ~ $Mg^{2+}$ (0 mol m$^{-2}$·hour$^{-1}$) (Fig. 2J). The synergistic effect of size sieving and electrostatic repulsions of Q(5%)-PEI(1.0)@ZIF could impede the divalent cations ($Ca^{2+}$ and $Mg^{2+}$) transport, where both $Ca^{2+}$ and $Mg^{2+}$ permeation rates decrease close to 0 mol m$^{-2}$·hour$^{-1}$. Through the pristine CEM, monovalent cations with smaller Stokes radii are preferentially transported, which means that $K^+$ is the easiest to be transported, followed by $Na^+$ and then $Li^+$ (*37*, *38*). However, our prepared Q(5%)-PEI(1.0)@ZIF#CEM shows a much enhanced $Li^+$ permeation rate instead, making the transport of $Li^+$ faster than $Na^+$ and close to that of $K^+$. This changed $Li^+$ transport behavior can be explained by $Li^+$ controlled Q(5%)-PEI(1.0)@ZIF structure formation and the bonding affinity of reacted ETAC. Consequently, this enhanced $Li^+$ ion permeation rate, together with high $Li^+/M^{z+}$ permselectivity of Q(5%)-PEI(1.0)@ZIF#CEM (Fig. 2K), could be used to achieve highly efficient $Li^+$ recovery from water streams.

Theoretically, the design principles of the Q(5%)-PEI(1.0)@ZIF#CEM membrane for cation selectivity are based on the electrical field–assisted $Li^+$ control synergizing with Donnan equilibrium, size sieving, electrostatic interaction, or bonding affinity (Fig. 3A): (i) Donnan equilibrium—Anion (i.e., $Cl^-$) can move into the positively charged cavity of Q(5%)-PEI(1.0)@ZIF but cannot transport through CEM; cations can transport from this cavity instead; (ii) electrostatic repulsion—Monovalent/multivalent cations is selectively separated; (iii) size sieving and dehydration—Smaller hydrated cations transport into the cavity with part-dehydration energy; (iv) electric field–assisted ion control—The $Li^+$ controlled ETAC formation of the Q(5%)-PEI(1.0)@ZIF forms well-defined geometrical and chemical channels enabling fast and precise $Li^+$ transport; (v) bonding affinity—Functional groups with high adsorption energy (i.e., bonding affinity) to $Li^+$ enhance $Li^+$ transport (figs. S16 to S19).

To investigate the $Li^+$ transport ability through the Q-PEI@ZIF structure, on the basis of the results of cations permeation ability through CEM and Q(5%)-PEI(1.0)@ZIF#CEM, we select representative monovalent ($Li^+$, $Na^+$, and $K^+$) and divalent ($Mg^{2+}$ and $Ca^{2+}$) cations to study their transport mechanisms. Among those ions, $Na^+$ and $Mg^{2+}$ are the mono- and divalent ion species that often interfere with $Li^+$ recovery from water streams (*39*), while $K^+$ and $Ca^{2+}$ are included to further validate the observed selectivity trend. The DFT calculations are performed to compare the bonding affinity (adsorption energy, $E_{ads}$) of these cation species on the Q-PEI@ZIF. In the calculations, the active part of the Q-PEI@ZIF framework (Fig. 3B) is referred to $Q^+$-PEI($Cl^-$), where several $Cl^-$ surround the $Q^+$-PEI molecule (Fig. 3C and table S3). This model is constructed to be consistent with experimental results. Multiple potential binding sites are considered for each ion species, and the most energetically favorable configurations are identified (figs. S20 to S25). As shown in Fig. 3D, the calculated $E_{ads}$ values indicate a clear difference between monovalent and divalent cations. $Li^+$ exhibits the strongest binding at −2.23 eV/ion, followed by $Na^+$ (−1.86 eV/ion) and $K^+$ (−1.55 eV/ion), while the divalent $Mg^{2+}$ and $Ca^{2+}$ show substantially weaker adsorption energies of −0.74t and −0.68 eV/ion, respectively. Further analyses reveal the differences in cation interaction with the $Q^+$-PEI($Cl^-$) framework. $Li^+$ forms a Li—N bond of 1.99 Å, close to the 2.03-Å bond length in cyclic $Li_2N_2$ (*40*, *41*). Charge density difference analysis reveals substantial electron accumulation between $Li^+$ and [N], confirming the strong

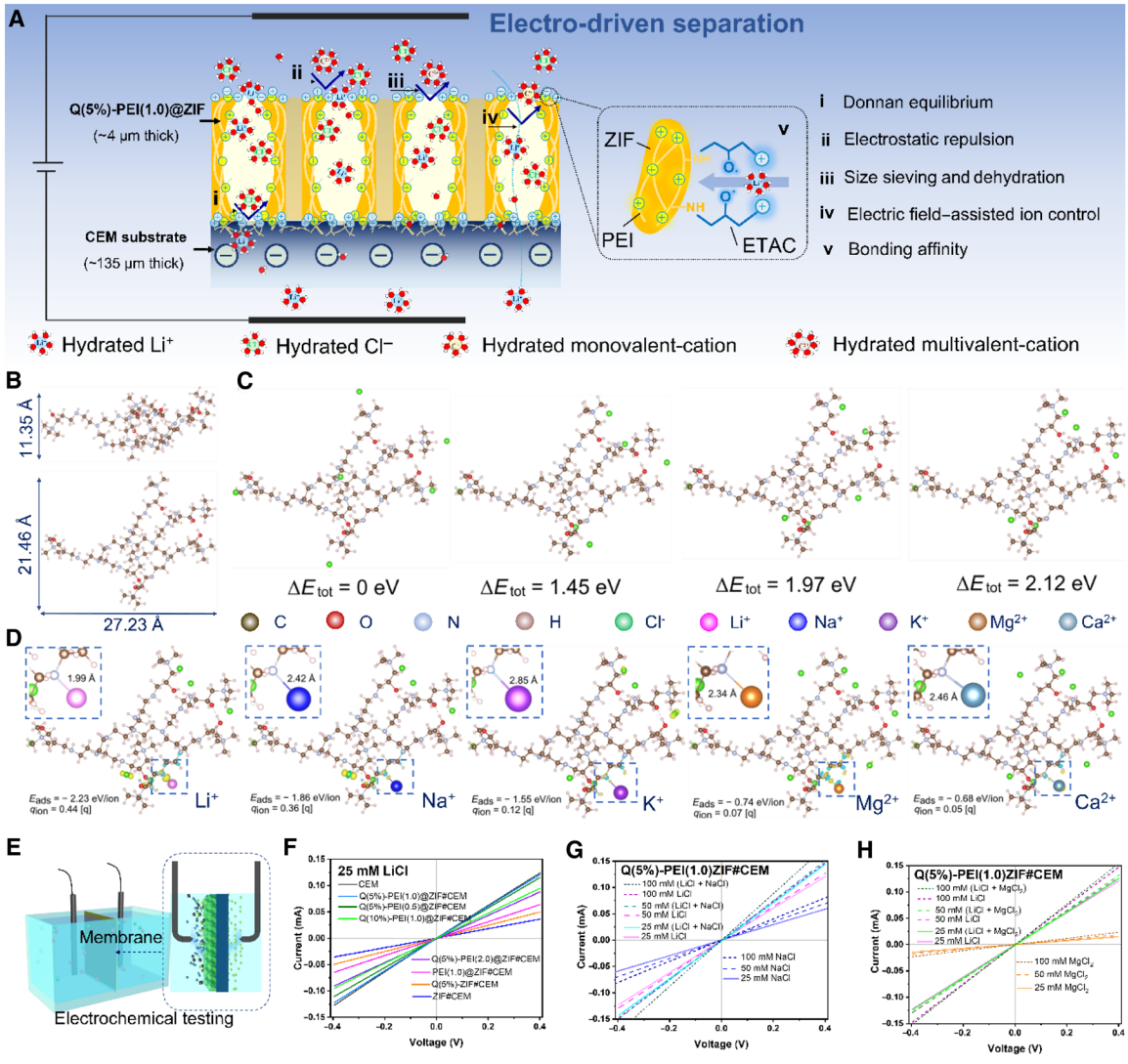



**Fig. 3. Ion transport mechanisms of the Q(5%)-PEI(1.0)@ZIF#CEM.** (**A**), Schematic illustration of the ion transport and selective separation behavior from the Q(5%)-PEI(1.0)@ZIF#CEM. (**B**) Basic molecular structure of Q-PEI@ZIF. (**C**) The structures and corresponding total energies of four cases of $Q^+$-PEI surrounded by six $Cl^-$. (**D**) The configuration and corresponding adsorption energy of $Li^+$, $Na^+$, $K^+$, $Mg^{2+}$, and $Ca^{2+}$ bonding affinity on $Q^+$-PEI($Cl^-$) at the most energetically favorable site. The inserted atomic structure shows the details of the adsorption configuration. The brown, silver, white, red, green, pink, blue, purple, orange, and cyan balls represent C, N, H, O, Li, Na, K, Mg, and Ca atoms. The isosurface level is set as 0.05 e/Å$^3$. (**E**) Schematic of the electro-driven cell used for ion transport measurements. (**F**) C-V characteristics of membranes measured under the electro-driven cell with 25 mM LiCl solution (pH 7.0). (**G** and **H**), C-V characteristics of the Q(5%)-PEI(1.0)@ZIF#CEM measured under an electric field with various solutions.

ionic character of this interaction. Similarly, $Na^+$ and $K^+$ bind to [N] with bond lengths of 2.42 and 2.85 Å, respectively, and exhibit clear ionic interactions as evidenced by charge accumulation between the cations and [N]. In contrast, $Mg^{2+}$ and $Ca^{2+}$ adsorb near [N] with bond distances of 2.34 and 2.46 Å, respectively, but exhibit only minimal electron accumulation, indicating much weaker interaction between the divalent cations and the framework at the binding sites (Fig. 3D). The substantially stronger bonding affinity between $Li^+$/$Na^+$/$K^+$ and $Q^+$-PEI($Cl^-$), compared to $Mg^{2+}$ or $Ca^{2+}$, originates from enhanced charge transfer between these cations and $Q^+$-PEI($Cl^-$). Bader charge analysis quantifies this effect, showing that $Li^+$, $Na^+$, and $K^+$ transfer 0.44, 0.36, and 0.31 elementary charges ([q]), respectively, while $Mg^{2+}$ and $Ca^{2+}$ transfer only 0.07 [q] and 0.05 [q] (table S4). The strong ionic bonding formed between monovalent cations and [N] sites highlights the high affinity of $Q^+$-PEI($Cl^-$) toward monovalent species, thereby explaining the superior selectivity for $Li^+$, $Na^+$, and $K^+$ over divalent ions in electrodialysis (Fig. 2, I and J). Among the monovalent ions, $Li^+$ shows the strongest binding, consistent with its superior transport performance, while $K^+$ exhibits slightly weaker adsorption energy than $Li^+$ and $Na^+$ in DFT calculations. Its experimental selectivity is comparable to $Li^+$, likely due to its smaller hydrated ion size and weaker interaction with the membrane, resulting in lower migration barriers. These synergetic effects in Q-PEI@ZIF perform the $K^+$ ~ $Li^+$ > $Na^+$ ion transport ability order of the resulting membrane under an applied electric field.

Current-voltage (C-V) characteristics of membranes in 25 mM LiCl, 25 mM NaCl, 25 mM $MgCl_2$, and 25 mM mixed solutions (i.e., LiCl/NaCl and LiCl/$MgCl_2$) are measured under the electric field, respectively, to describe the dynamic behavior of ion conductivities (Fig. 3E). In 25 mM LiCl, all the prepared membranes present different C-V characteristic slopes (Fig. 3F). These varying C-V characteristics are used for mimicking the $Li^+$ transport properties of prepared constructions and composed of different ion conductivities, demonstrating that the Q-PEI@ZIF has high $Li^+$ transport ability. To further demonstrate the electrical field–assisted ion control in synergistic principles on this distinct cation-selective construction, the C-V characteristic of these membranes is evaluated in 25 mM NaCl and 25 mM $MgCl_2$ (figs. S26 and S27). In contrast, all the Q-PEI@ZIF constructions show lower $Na^+$ transport abilities and almost no $Mg^{2+}$ transport abilities from the C-V conductivity characteristic slope, while the Q(5%)-PEI(1.0)@ZIF#CEM shows a much higher $Li^+$ transport ability. Figure 3 (G and H) shows the C-V characteristics of Q(5%)-PEI(1.0)@ZIF#CEM in different solutions. These C-V characteristic slopes in LiCl or binary solutions containing $Li^+$ are much higher than those in unary NaCl or $MgCl_2$ solutions, which indicates that this highly conductive phenomenon is mainly caused by the superior $Li^+$ transport ability.

To investigate the ion transport ability through the Q-PEI@ZIF structure, here, a binary ion solution is chosen to simplify and investigate the ion transport mechanism. The membrane selectivity of $Li^+/Mg^{2+}$ in a mixed aqueous solution is further explored in electrodialysis by using as-prepared membranes, at varying $Li^+$ and $Mg^{2+}$ initial concentrations and $Li^+/Mg^{2+}$ ratios (Fig. 4A). In electrodialysis (i.e., current density of 5.0 mA·$cm^{-2}$, 100 ml of 25 mM initial $Li^+/Mg^{2+}$ mixtures in both dilute and concentrated chambers), the concentrations of both $Li^+$ and $Mg^{2+}$ increases in a similar trend to the concentrate chamber through the pristine CEM (Fig. 4B). In contrast, all ZIF-based CEMs show different trends of $Li^+$ and $Mg^{2+}$ under the same operating conditions (figs. S28 to S35). The ZIF#-CEM, designed only on the basis of size sieving effects, leads to both lower $Li^+$ and $Mg^{2+}$ transport, although $Li^+$ can be separated from $Mg^{2+}$ by the ZIFs (fig. S29). In contrast to the ZIF#CEM, the ionized ZIF-based membranes show not only high $Li^+$ concentration in the concentrated chamber but also low $Mg^{2+}$ in 120 min (figs. S28 to S35). In particular, the Q(5%)-PEI(1.0)@ZIF#CEM achieves the same $Li^+$ increased value (20.0 mM) as the pristine CEM (20.5 mM) in 120 min, while almost no increase of $Mg^{2+}$ in the concentrate chamber was observed (Fig. 4B). Under the same operating conditions, different increasing trends of the $Mg^{2+}$ and $Li^+$ through these membranes reflect varying ion transport behaviors, which is mainly due to the presence of ZIFs and the Q-PEI fixed in ZIFs.

The ion permeability (Fig. 4C) and $Li^+/Mg^{2+}$ permselectivity (Fig. 4D) of CEM, ZIF#CEM, and Q(5%)-PEI(1.0)@ZIF#CEM were investigated to assess $Mg^{2+}$ and $Li^+$ transport behavior through membranes. The Q(5%)-PEI(1.0)@ZIF#CEM yields an ion permeation rate of 0.50 mol $m^{-2}$·$hour^{-1}$ for $Li^+$ during 120 min of testing, which is comparable to the pristine CEM (i.e., 0.52 mol $m^{-2}$·$hour^{-1}$). However, $Mg^{2+}$ cannot pass into the recovery chamber through Q(5%)-PEI(1.0)@ZIF#CEM, with an ion permeation rate of 0 mol $m^{-2}$·$hour^{-1}$. Thus, an extremely high $Li^+/Mg^{2+}$ permselectivtity of 20,000 can be achieved with Q(5%)-PEI(1.0)@ZIF#CEM, while the $Li^+/Mg^{2+}$ permselectivtity of pristine CEM is as low as 0.99. This phenomenon is probably because of the $Li^+$ control of the ionized structure. Because of the positively charged groups fixed within the $Li^+$ controlled structure, the $Cl^-$ enters into Q(5%)-PEI(1.0)@ZIF cavity by electrostatic attraction so that $Li^+$ can easily transport through this structure via the Donnan equilibrium and the electron double layer. The ZIF#CEM demonstrates a decreased $Li^+$ permeation rate, although the $Li^+/Mg^{2+}$ permselectivity is slightly improved compared to pristine CEM. Thus, on the basis of the electric field–assisted assembly strategy and synergistic separation principles of size sieving, electrostatic interaction, and bonding affinity, the Q(5%)-PEI(1.0)@ZIF#CEM has a high $Li^+/Mg^{2+}$ permselectivity and a high $Li^+$ permeation rate in an electro-driven process. Accordingly, this high $Li^+$ ion permeation rate together with the high $Li^+/Mg^{2+}$ permselectivity can make the purity of $Li^+$ in the concentrate chamber reach >99.99% in 120 min, while it is only 63.55% of ZIF#CEM and 49.88% for the pristine CEM (Fig. 4E). Compared to the most advanced membranes reported to date, the Q(5%)-PEI(1.0)@ZIF#CEM sets a benchmark by achieving unparalleled $Li^+/Mg^{2+}$ permselectivity while maintaining an excellent balance in $Li^+$ permeation rate, thereby overcoming the permeation-selectivity tradeoffs (Fig. 4F and table S5) (*14*, *42*–*49*). Consequently, superior $Li^+$ recovery rate and $Li^+$ purity are achieved by using the Q(5%)-PEI(1.0)@ZIF#CEM in electrodialysis compared to other $Li^+$ recovery systems (Fig. 4G and table S6) (*50*–*60*).

Considering that different water streams may have different salt concentrations as well as ion ratios, the effect of salt concentration ($Mg^{2+}$ and $Li^+$) on the Q(5%)-PEI(1.0)@ZIF#CEM performance is comprehensively studied. With increasing concentration of the mixed solution from 25 mM to 100 mM, the $Li^+$ permeation rate increases from 0.50 to 0.80 mol $m^{-2}$·$hour^{-1}$ (Fig. 4H and fig. S36), while the $Li^+/Mg^{2+}$ permselectivity (in 120 min) decreases from 20,000 to 10 (Fig. 4I). This is because the high ion concentration could increase the current efficiency, enhancing transport of both $Mg^{2+}$ and $Li^+$. Figure 4J shows the effect of the $Li^+/Mg^{2+}$ ratio of 1:1, 1:10, and 1:100 on $Li^+/Mg^{2+}$ permselectivity, the $Li^+/Mg^{2+}$ permselectivity of Q(5%)-PEI(1.0)@ZIF#CEM decreases from 100 to 60 and 30, respectively. During this process, the $Mg^{2+}$ permeation rate remains constant because of the fixed concentration, while the $Li^+$ is substantially reduced at a lower concentration (fig. S37). Thus, it consequently causes a decreasing $Li^+/Mg^{2+}$ permselectivity with decreasing $Li^+/Mg^{2+}$ ratios.

## DISCUSSION

On the basis of the hypothesis of electric field–assisted ion control and the synergistic principles of size sieving, electrostatic interaction, and bonding affinity, this work constructs an ionized MOF functionalized layer on a CEM surface. The as-developed membrane shows an ultraefficient transport trend of $Li^+$. In electrodialysis, the resulting membrane has the following order of ion transport ability: $K^+ \sim Li^+ > Na^+ > Ca^{2+} \sim Mg^{2+}$. Supported by DFT calculations (based on electrostatic interactions analysis) and ion conductivity testing (based on dynamic experimental analysis), it confirms that the Q(5%)-PEI(1.0)@ZIF#CEM membrane has a stronger affinity and enhanced transport ability for $Li^+$ compared to $Na^+$ and $Mg^{2+}$. In 5 mA·$cm^{-2}$ electrodialysis, with 25 mM initial $Li^+/Mg^{2+}$ mixture, the Q(5%)-PEI(1.0)@ZIF#CEM membrane exhibits the $Li^+/Mg^{2+}$ permselectivity as high as 20,000. The purity of $Li^+$, 99.99%, is obtained by 120 min of electrodialysis. The design concept,

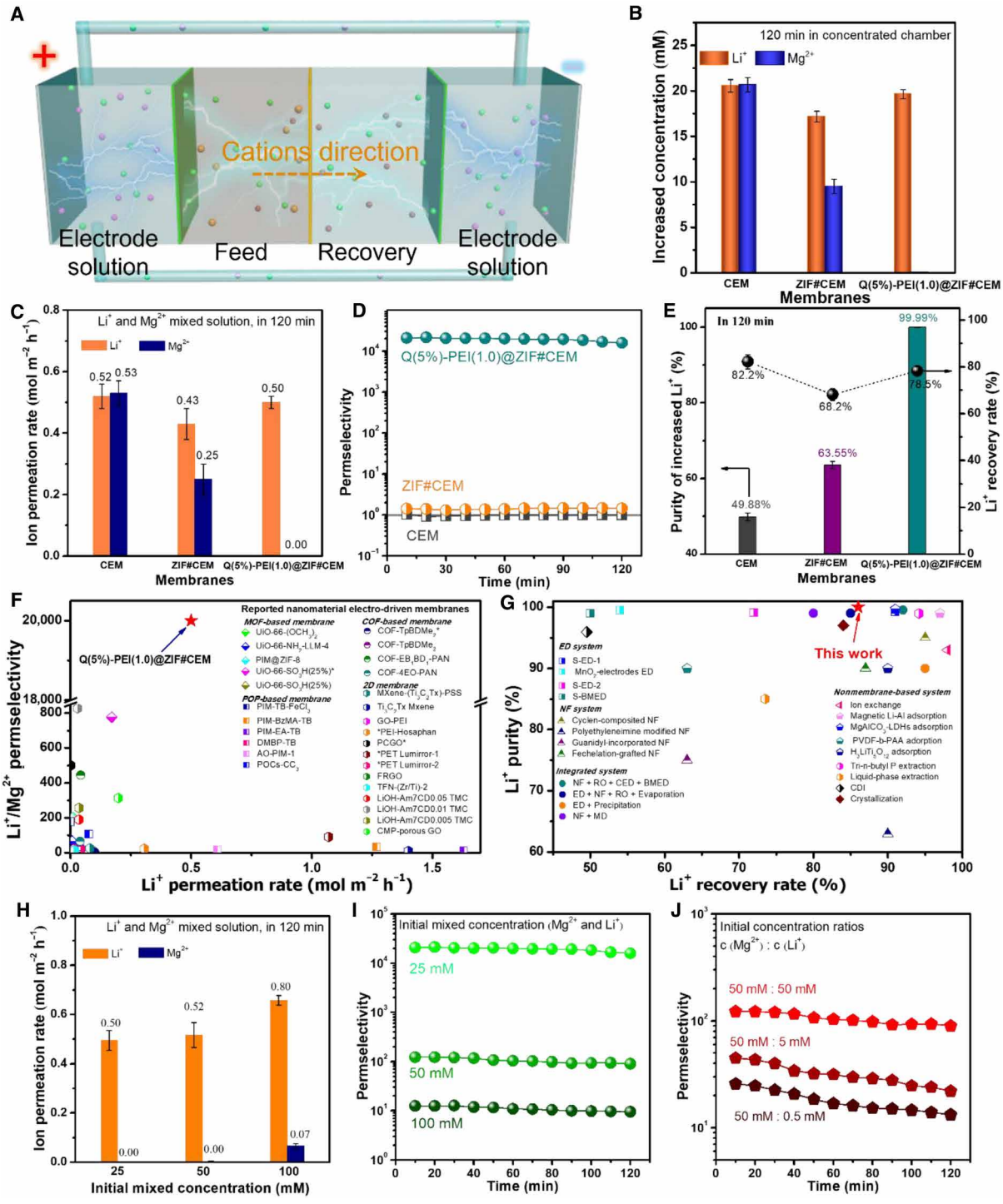



**Fig. 4. Lithium resource recovery from the $Mg^{2+}$ and $Li^{+}$ mixed solutions.** (**A**) Scheme of membrane selectivity of $Li^{+}/Mg^{2+}$ in electrodialysis (i.e., the current density of 5.0 mA·cm$^{-2}$, 100 ml of 25 mM initial $Li^{+}/Mg^{2+}$ mixtures in both dilute and recovery chambers). (**B**) Increased concentrations of $Mg^{2+}$ and $Li^{+}$ in the recovery chamber in 120 min via the CEM, ZIF#CEM, and Q(5%)-PEI(1.0)@ZIF#CEM. (**C**) Ion permeation rate of $Mg^{2+}$ and $Li^{+}$ during 120 min of CEM, ZIF#CEM, and Q(5%)-PEI(1.0)@ZIF#CEM membranes. (**D**) The permselectivity values of the CEM, ZIF#CEM, and Q(5%)-PEI(1.0)@ZIF#CEM membranes during 120 min. (**E**) The $Li^{+}$ purity and recovery rate by CEM, ZIF#CEM, and Q(5%)-PEI(1.0)@ZIF#CEM membranes. (**F**) Comparison of $Li^{+}/Mg^{2+}$ permselectivity and $Li^{+}$ permeation rate of the Q(5%)-PEI(1.0)@ZIF#CEM membrane with other reported nanomaterial electro-driven membranes, including polymeric MOF-based membranes, COF-based membranes, POPs membranes, and 2D membranes. (**G**) Comparison of $Li^{+}$ recovery rate and $Li^{+}$ recovery purity of this work with other reported systems, including electrodialysis, nanofiltration, integrated membrane system, and non-membrane system (Operated conditions are shown in table S6). (**H**) Ion permeation rate of $Mg^{2+}$ and $Li^{+}$ in 120 min of Q(5%)-PEI(1.0)@ZIF#CEM membranes with initial concentrations of 25, 50, and 100 mM, respectively. (**I** and **J**) $Li^{+}/Mg^{2+}$ permselectivity values of the Q(5%)-PEI(1.0)@ZIF#CEM with different initial concentrations (25, 50, and 100 mM) and with different initial concentration ratios [50 mM of n($Mg^{2+}$):n($Li^{+}$) = 1:1, 10:1, and 100:1, respectively]. h, hours.

technological principle, and evaluation methods will expand the electric field–assisted $Li^+$ control in the construction of an ionized framework for highly efficient recovery of ion resources.

## MATERIALS AND METHODS

### Chemicals and membranes

2-methylimidazole (99%), $Zn(NO_3)_2{\cdot}6H_2O$, polyethyleneimine ($M_w = 2000$), ETAC, DMP-30, lithium chloride (LiCl), sodium chloride (NaCl), sodium chloride (NaCl), potassium chloride (KCl), magnesium chloride ($MgCl_2$), calcium chloride ($CaCl_2$), and sodium sulfate ($Na_2SO_4$) were purchased from the Sigma-Aldrich (Germany). All the chemicals were used without any further purification. In this work, the Fujifilm commercial anion exchange membrane (type I) and CEM (type I) were used to support this study (in table S1).

### Preparation of the Q-PEI@ZIF#CEM membranes

In this study, the Q-PEI@ZIF crystals are constructed via the PEI threaded ZIF (PEI@ZIF) through an in situ confinement conversion process and the ETAC quaternized PEI@ZIF (Q-PEI@ZIF) via an alternating current electric field–assisted $Li^+$ control assembly process (*27*). The commercial CEM (pristine CEM) is immersed in a 2-methylimidazole solution and kept in a horizontal placement state. Different contents of positively charged PEI mixed with the $Zn(NO_3)_2{\cdot}6H_2O$ are added and added into this 2-methylimidazole solution (volume ratio 1:2). Then, the PEI@ZIF crystals are assembled on the pristine CEM surface, and the first PEI@ZIF layer on CEM surface based on in situ growth and electrostatic bonding interaction is constructed. Then, the defective PEI@ZIF layer is eliminated by repeating the construction of PEI@ZIF crystals. Last, the PEI@ZIF#CEM with ample -$NH_2$ groups is placed perpendicular to a laboratory-designed membrane assembly device (an electric field–assisted ion control membrane assembly device, i.e., eF-IC membrane device). In theory, the -$NH_2$ in PEI@ZIF can react with the epoxy group in ETAC under the catalyst of DMP-30. Thus, the positively charged ETAC mixed with LiCl solution is added into the above eF-IC membrane device and is chemically assembled in the PEI@ZIF structure with activation of the DMP-30 catalyst. In this process, the $Li^+$ can not only transport the PEI@ZIF#CEM but also affect the ETAC monomers assembly on PEI@ZIF architectures, obtaining the Q-PEI@ZIF layer on the pristine CEM surface. In addition, unstable stacked Q-PEI@ZIF crystals can fall from the layers under this alternating-current electric field (10 V, 50 Hz). After that, only the stable and thin Q-PEI@ZIF crystals are constructed on pristine CEM.

### Characterization methods

#### *Chemical characterization*

All the samples were dried thoroughly in a vacuum oven at 45°C for 24 hours. The total reflectance ATR-FTIR (Nicolet 6700, USA) is used to monitor the functional groups of Q-PEI@ZIF crystals and membranes. XPS (Kratos AXIS Ultra DLD, Japan) with a current of 1.8 A, bias 3.3 V and bias 1.0 V is used to analyze the elemental compositions of the synthesized Q-PEI@ZIF crystal samples. The high resolution of Q-PEI@ZIF crystals is also characterized by XPS.

#### *Structure characterization*

Photographs are taken with a digital camera. The morphologies of Q-PEI@ZIF crystals and membranes, including surface and cross section, are observed with an SEM (S-4700 Hitachi, Tokyo, Japan) at an accelerating voltage of 10.0 kV. The surface roughness of the Q-PEI@ZIF crystals (the scanning area is 1 μm by 1 μm of each sample) and membranes (the scanning area is 5 μm by 5 μm of each sample) is evaluated by an AFM (Bruker, USA) under tapping mode at 25°C. Powder XRD Bruker D2 Phaser, USA) is used to record the structure changes between Q-PEI@ZIF and ZIF-L crystals with a scanning speed of 2.0° per minute at 25°C. The BET adsorption isotherms of Q(5%)-PEI(1.0)@ZIF and ZIF are measured at standard temperature and pressure (273 K and 101.325 kPa, respectively with $N_2$) by using surface area and pore size analyzer (Quantachrome NOVA 2200E BET, USA) for surface area, pore volume, and pore size distribution.

### Electrochemical properties

Surface charge density of the CEM, ZIF#CEM, and Q(5%)-PEI(1.0)@ZIF#CEM are calculated via streaming potential measurements by an electro-kinetic analyzer (Anton Paar, Graz, Austria) at pH 7, where a 1.0 mM KCl solution is passed over the membrane surface. Surface electrical resistance ($R_S$) of pristine CEM and prepared membranes is measured in 0.50 M NaCl. The electrode solution for testing is 0.2 M $Na_2SO_4$ (*61*). Before testing, all membranes have been immersed in 0.5 M NaCl solution for 8 hours. Membrane surface electrical resistance $R_S$ (ohm·cm$^2$) is calculated as

$$R_S = \frac{U - U_0}{I} \times S$$

where $U$ and $U_0$ (V) are the voltage with and without membrane samples, respectively; $I$ (0.04 A) is the constant current through the membranes. S (7.065 cm$^2$) is the membrane area.

Polarization C-V curves of all membranes are tested in 0.10 M NaCl in electrodialysis. Before testing, these Q-PEI@ZIF#CEM membranes are immersed in a 0.1 M NaCl solution for 8 hours. The membrane surface current density, $I_s$ (A·cm$^{-2}$) is calculated by

$$I_s = \frac{I}{s}$$

where I (A) is the current through the membranes and s (7.065 cm$^2$) is the membrane area.

The dynamic behavior of membrane ion conductivities is evaluated through the C-V characteristics in 25 mM LiCl, 25 mM $MgCl_2$, and 25 mM mixed solutions (pH 7.0), respectively, in the laboratory-designed testing device. An electrochemical workstation (Autolab PGSTAT 302 N, Metrohm Belgium) is used to measure the Q-PEI@ZIF#CEM membranes (7.065 cm$^2$), and the scale of voltage is −0.4 V to 0.4 V.

### Ion-selective measurements

#### *Multi-cation mixed system*

The temporal evolution of multi-cations ($Li^+$, $Na^+$, $K^+$, $Ca^{2+}$, and $Mg^{2+}$) concentrations in electrodialysis is measured to evaluate the ion-selective performance, including ion permeation rate and $Li^+/M^{z+}$ permselectivity (fig. S38). The initial composition of solutions both in feed and recovery chambers is 25 mM mixed solutions (i.e., LiCl, NaCl, KCl, $MgCl_2$, and $CaCl_2$). The effective area of the membrane sample is 19.625 cm$^2$, and the application of constant current is 0.10 A, with the membrane surface current of 5.0 mA·cm$^{-1}$. The electrode solution is 300 ml of 0.5 M NaCl. Every 10 min, the concentration of $Li^+$, $Na^+$, $K^+$, $Ca^{2+}$, and $Mg^{2+}$ in the recovery chamber is analyzed by inductively coupled plasma optical emission spectrometry (ICP-OES, Thermo Fisher Scientific iCAP 7400 Duo, USA). The limit of detection is calculated from the variance in the background signal relative to the standard line (table S7).

***Binary-cation mixed system***

The temporal evolution of binary-cation ($Li^+$ and $Mg^{2+}$) concentrations in electrodialysis is measured to explore the ion-selective mechanisms (fig. S38). The initial composition of solutions both in feed and recovery chambers is 25 mM mixed solutions (i.e., LiCl and $MgCl_2$), and the concentration of $Li^+$ and $Mg^{2+}$ in the recovery chamber is measured every 10 min by ICP-OES (*62*).

***Ion permeation rate (J)***

It is used to illustrate ion transport ability, which is the ion permeation rate and expressed in $mol{\cdot}m^{-2}{\cdot}hour^{-1}$. It is calculated as

$$J = \frac{V \cdot \frac{dc}{dt}}{S}$$

where $c$ is the ion concentration; $V$ (100 mL) is the volume of solution, and S (20 $cm^2$) is the membrane area.

***Permselectivity (P)***

It is used to illustrate membrane selectivity compared to other ions. When the permselectivity >1, it indicates the selective property between two ions. Otherwise, it suggests no selectivity. Compared to other cations ($M^{z+}$), the $Li^+$/ $M^{z+}$ permselectivity is calculated as

$$P_M^{Li} = \frac{T_{Li} / T_M}{c_{Li} / c_M} = \frac{J_{Li} \cdot c_M}{J_M \cdot c_{Li}}$$

where $T$ is the ion transport number.

## DFT calculation

The DFT calculations are performed by using the Vienna ab initio simulation package (*63*). We adopt the generalized gradient approximation implemented by Perdew, Burke, and Ernzerhof and the projector augmented wave approach (*64*, *65*). The C($2s^22p^2$), N($2s^22p^3$), H($1s^1$), O($2s^22p^4$), Cl($3s^23p^5$), Li($2s^1$), Na($3s^1$), K($3s^23p^64s^1$), Mg($3s^2$), and Ca($3s^23p^64s^2$) valence states are used to describe electron-nuclear interact. The plane-wave basis cutoff is set as 400 eV. The energy convergence criterion is set to $10^{-5}$ eV, and the residual forces in the converged structures are smaller than 0.01 eV/Å. The Brillouin zone is sampled by a single gamma. The branched PEI polymer is placed in a simulation cell of 50 Å by 50 Å by 30 Å, providing over 15 Å of vacuum spacing in all directions to eliminate spurious interactions between periodic images.

To investigate the intrinsic ion selectivity behavior, we model a positively charged $Q^+$-PEI polymer segment in vacuum, neglecting explicit solvent and background electrolyte. To mimic the ionized state of the polymer, a positively charged $Q^+$-PEI segment is modeled in vacuum without explicit solvent or background electrolyte, and $Cl^-$ counterions are introduced to achieve charge balance and stabilize the configuration. Table S3 shows the charge of different element species in both Q-PEI and ionized $Q^+$-PEI($Cl^-$). Before the introduction of $Cl^-$, the Q-PEI remains electrically neutral. While $Cl^-$ is introduced in the system, the Q-PEI is positively charged, forming ionized $Q^+$-PEI as $Cl^-$ transfers 0.831 elementary electrons ([q]) to Q-PEI. To find the adsorption sites for $Cl^-$ surrounding $Q^+$-PEI, we calculate the bonding affinity (adsorption energy, $E_{ads}$) of $Cl^-$ by

$$E_{ads}(Cl) = E_{total} - E_{Q-PEI} - E_{Cl}$$

where $E_{total}$, $E_{Q\text{-}PEI}$, and $E_{Cl}$ are the total energy of $Cl^-$ adsorbed on Q-PEI, the total energy of Q-PEI, and the total energy of the $Cl^-$ in a vacuum, respectively. $Cl^-$ has the most negative adsorption energy of −0.36 eV/ion when positioned at the top site of H, which is connected to O. Consequently, we place six $Cl^-$ surrounding $Q^+$-PEI($Cl^-$) to maintain the coordination of N atoms in the polymer line. Figure 3C summarizes four cases of $Q^+$-PEI($Cl^-$) surrounded by six $Cl^-$, and the case with the most negative total energy was selected as the ground state of ionized $Q^+$-PEI($Cl^-$).

The $Q^+$-PEI($Cl^-$) structure is treated as rigid (atomic positions fixed) during cation adsorption calculations, while $Li^+$/$Na^+$/$K^+$/$Mg^{2+}$/$Ca^{2+}$ ions are allowed to relax freely. This approach isolates the energetic contributions from ion-polymer interactions and neglects polymer reorganization and entropic contributions. The bonding affinity energy ($E_{ads}$) of surface species is calculated by

$$E_{ads}(M) = E_{total} - E_{Q^+\text{-}PEI(Cl^-)} - E_M$$

where $E_{total}$, $E_{Q^+\text{-}PEI(Cl^-)}$, and $E_M$ are the total energy of cation adsorbed on $Q^+$-PEI($Cl^-$), the total energy of the state $Q^+$-PEI($Cl^-$), and the total energy of the cation atom in a vacuum, respectively. Figures S21 to S25 summarizes the configurations and corresponding adsorption energies of $Li^+$/$Na^+$/$K^+$/$Mg^{2+}$/$Ca^{2+}$ at other adsorption sites. To model the ionic forms ($Li^+$, $Na^+$, $K^+$, $Mg^{2+}$, and $Ca^{2+}$), we introduced additional $Cl^-$ ions into the system to achieve charge neutrality and mimic realistic ionized states. We also performed calculations using neutral Li, Na, and Mg atoms and observed similar adsorption trends (table S8). Figures S39 to S42 summarize the configurations and corresponding adsorption energies of Li/Na/Mg atoms at various adsorption sites. Van der Waals interactions are included via the DFT-D3 method to account for weak dispersion forces (*66*). Adsorption energies were computed at 0 K based on static total energy differences, under the assumption that enthalpic interactions dominate the observed ion selectivity.

## Supplementary Materials

**This PDF file includes:**

Supplementary Methods
Figs. S1 to S42
Tables S1 to S8

## REFERENCES AND NOTES


1. B. Swain, Recovery and recycling of lithium: A review. *Sep. Purif. Technol.* **172**, 388–403 (2017).
2. W. J. Koros, C. Zhang, Materials for next-generation molecularly selective synthetic membranes. *Nat. Mater.* **16**, 289–297 (2017).
3. R. Wang, J. Zhang, C. Y. Tang, S. Lin, Understanding selectivity in solute-solute separation: Definitions, measurements, and comparability. *Environ. Sci. Technol.* **56**, 2605–2616 (2022).
4. Q. Yang, Y. Su, C. Chi, C. T. Cherian, K. Huang, V. G. Kravets, F. C. Wang, J. C. Zhang, A. Pratt, A. N. Grigorenko, F. Guinea, A. K. Geim, R. R. Nair, Ultrathin graphene-based membrane with precise molecular sieving and ultrafast solvent permeation. *Nat. Mater.* **16**, 1198–1202 (2017).
5. P. Zuo, C. Ye, Z. Jiao, J. Luo, J. Fang, U. S. Schubert, N. B. McKeown, T. L. Liu, Z. Yang, T. Xu, Near-frictionless ion transport within triazine framework membranes. *Nature* **617**, 299–305 (2023).
6. A. Battistel, M. S. Palagonia, D. Brogioli, F. La Mantia, R. Trocoli, Electrochemical methods for lithium recovery: A comprehensive and critical review. *Adv. Mater.* **32**, e1905440 (2020).
7. Y. Zhao, N. Mamrol, W. A. Tarpeh, X. Yang, C. Gao, B. Van der Bruggen, Advanced ion transfer materials in electro-driven membrane processes for sustainable ion-resource extraction and recovery. *Prog. Mater. Sci.* **128**, 100958 (2022).
8. Y. Zhao, M. Wu, P. Shen, C. Uyterhoeven, N. Mamrol, J. Shen, C. Gao, B. Van der Bruggen, Composite anti-scaling membrane made of interpenetrating networks of nanofibers for selective separation of lithium. *J. Membrane Sci.* **618**, 118668 (2021).
9. H. Peng, W. H. Zhang, W. S. Hung, N. Wang, J. Sun, K. R. Lee, Q. F. An, C. M. Liu, Q. Zhao, Phosphonium modification leads to ultrapermeable antibacterial polyamide composite membranes with unreduced thickness. *Adv. Mater.* **32**, e2001383 (2020).

10. X. Tong, S. Liu, Y. Zhao, L. Huang, J. Crittenden, Y. Chen, MXene composite membranes with enhanced ion transport and regulated ion selectivity. *Environ. Sci. Technol.* **56**, 8964–8974 (2022).
11. G. Pace, O. Nordness, K. Asham, R. J. Clément, R. A. Segalman, Impact of side chain chemistry on lithium transport in mixed ion–electron-conducting polymers. *Chem. Mater.* **34**, 4672–4681 (2022).
12. M. Abdollahzadeh, M. Chai, E. Hosseini, M. Zakertabrizi, M. Mohammad, H. Ahmadi, J. Hou, S. Lim, A. Habibnejad Korayem, V. Chen, M. Asadnia, A. Razmjou, Designing angstrom-scale asymmetric MOF-on-MOF cavities for high monovalent ion selectivity. *Adv. Mater.* **34**, e2107878 (2022).
13. Y. Guo, Y. Ying, Y. Mao, X. Peng, B. Chen, Polystyrene sulfonate threaded through a metal–organic framework membrane for fast and selective lithium-ion separation. *Angew. Chem. Int. Ed. Engl.* **55**, 15120–15124 (2016).
14. F. Sheng, B. Wu, X. Li, T. Xu, M. A. Shehzad, X. Wang, L. Ge, H. Wang, T. Xu, Efficient ion sieving in covalent organic framework membranes with sub-2-nanometer channels. *Adv. Mater.* **33**, e2104404 (2021).
15. F. Soyekwo, H. Wen, D. Liao, C. Liu, Nanofiltration membranes modified with a clustered multiquaternary ammonium-based ionic liquid for improved magnesium/lithium separation. *ACS Appl. Mater. Interf.* **14**, 32420–32432 (2022).
16. Y. K. Rongming Xu, W. Zhang, X. Zhang, B. Pan, Oriented UiO-67 metal–organic framework membrane with fast and selective lithium-ion transport. *Angew. Chem. Int. Ed. Engl.* **134**, e202115443 (2022).
17. H. N. Abdelhamid, Biointerface between ZIF-8 and biomolecules and their applications. *Biointerface Res. App. Chem.* **11**, 8283–8297 (2020).
18. M. Jian, R. Qiu, Y. Xia, J. Lu, Y. Chen, Q. Gu, R. Liu, C. Hu, J. Qu, H. Wang, X. Zhang, Ultrathin water-stable metal-organic framework membranes for ion separation. *Sci. Adv.* **6**, eaay3998 (2020).
19. R. Tan, A. Wang, R. Malpass-Evans, R. Williams, E. W. Zhao, T. Liu, C. Ye, X. Zhou, B. P. Darwich, Z. Fan, L. Turcani, E. Jackson, L. Chen, S. Y. Chong, T. Li, K. E. Jelfs, A. I. Cooper, N. P. Brandon, C. P. Grey, N. B. McKeown, Q. Song, Hydrophilic microporous membranes for selective ion separation and flow-battery energy storage. *Nat. Mater.* **19**, 195–202 (2020).
20. M. F. Jimenez-Solomon, Q. Song, K. E. Jelfs, M. Munoz-Ibanez, A. G. Livingston, Polymer nanofilms with enhanced microporosity by interfacial polymerization. *Nat. Mater.* **15**, 760–767 (2016).
21. A. Razmjou, M. Asadnia, E. Hosseini, A. Habibnejad Korayem, V. Chen, Design principles of ion selective nanostructured membranes for the extraction of lithium ions. *Nat. Commun.* **10**, 5793 (2019).
22. S. H. Park, S. J. Lee, Versatile amorphous structures of phosphonate metal−organic framework/alginate composite for tunable sieving of ions. *Adv. Funct. Mater.* **29**, 1904016 (2019).
23. Y. Zhang, X. Feng, H. Li, Y. Chen, J. Zhao, S. Wang, L. Wang, B. Wang, Photoinduced postsynthetic polymerization of a metal-organic framework toward a flexible stand-alone membrane. *Angew. Chem. Int. Ed. Engl.* **54**, 4259–4263 (2015).
24. R. Zhang, S. Ji, N. Wang, L. Wang, G. Zhang, J. R. Li, Coordination-driven in situ self-assembly strategy for the preparation of metal-organic framework hybrid membranes. *Angew. Chem. Int. Ed. Engl.* **53**, 9775–9779 (2014).
25. Y. Zhao, M. Wu, Y. Guo, N. Mamrol, X. Yang, C. Gao, B. Van der Bruggen, Metal-organic framework based membranes for selective separation of target ions. *J. Membrane Sci.* **634**, 119407 (2021).
26. W. H. Zhang, M. J. Yin, Q. Zhao, C. G. Jin, N. Wang, S. Ji, C. L. Ritt, M. Elimelech, Q. F. An, Graphene oxide membranes with stable porous structure for ultrafast water transport. *Nat. Nanotechnol.* **16**, 337–343 (2021).
27. L. Xia, Y. Zhao, X. Zhang, Y. Qiu, J. Shao, R. Dewil, B. V. der Bruggen, X. Yang, Ionic control of functional zeolitic imidazolate framework-based membrane for tailoring selectivity toward target ions. *ACS Appl. Mater. Interf.* **14**, 11038–11049 (2022).
28. Y. Zhao, Y. Liu, C. Wang, E. Ortega, X. Wang, Y. F. Xie, J. Shen, C. Gao, B. Van der Bruggen, Electric field-based ionic control of selective separation layers. *J. Mater. Chem. A* **8**, 4244–4251 (2020).
29. T. Mei, H. Zhang, K. Xiao, Bioinspired artificial ion pumps. *ACS Nano* **16**, 13323–13338 (2022).
30. R. Xu, Y. Kang, W. Zhang, B. Pan, X. Zhang, Two-dimensional MXene membranes with biomimetic sub-nanochannels for enhanced cation sieving. *Nat. Commun.* **14**, 4907 (2023).
31. K. Cherukumilli, M. Steiner, J. R. Ray, Effective fluoride removal using granular bauxite filter media as an affordable and sustainable alternative to activated alumina. *Environ. Sci. Water Res. Technol.* **7**, 1465–1479 (2021).
32. Z. Zhang, X.-Y. Kong, G. Xie, P. Li, K. Xiao, L. Wen, L. Jiang, "Uphill" cation transport: A bioinspired photo-driven ion pump. *Sci. Adv.* **2**, e1600689 (2016).
33. M. Li, Y. Shen, K. Luo, Q. An, P. Gao, P. Xiao, Y. Zou, Harnessing dislocation motion using an electric field. *Nat. Mater.* **22**, 958–963 (2023).
34. Y. Zhao, Z. Mai, P. Shen, E. Ortega, J. Shen, C. Gao, B. Van der Bruggen, Nanofiber based organic solvent anion exchange membranes for selective separation of monovalent anions. *ACS Appl. Mater. Interf.* **12**, 7539–7547 (2020).
35. A. Deacon, L. Briquet, M. Malankowska, F. Massingberd-Mundy, S. Rudić, T. L. Hyde, H. Cavaye, J. Coronas, S. Poulston, T. Johnson, Understanding the ZIF-L to ZIF-8 transformation from fundamentals to fully costed kilogram-scale production. *Commun. Chem.* **5**, 18 (2022).
36. J. Shen, Y. Cai, C. Zhang, W. Wei, C. Chen, L. Liu, K. Yang, Y. Ma, Y. Wang, C. C. Tseng, J. H. Fu, X. Dong, J. Li, X. X. Zhang, L. J. Li, J. Jiang, I. Pinnau, V. Tung, Y. Han, Fast water transport and molecular sieving through ultrathin ordered conjugated-polymer-framework membranes. *Nat. Mater.* **21**, 1183–1190 (2022).
37. Y. Zhao, Y. Li, S. Yuan, J. Zhu, S. Houtmeyers, J. Li, R. Dewil, C. Gao, B. Van der Bruggen, A chemically assembled anion exchange membrane surface for monovalent anion selectivity and fouling reduction. *J. Mater. Chem. A* **7**, 6348–6356 (2019).
38. T. Luo, S. Abdu, M. Wessling, Selectivity of ion exchange membranes: A review. *J. Membrane Sci.* **555**, 429–454 (2018).
39. H. Peng, Q. Zhao, A nano-heterogeneous membrane for efficient separation of lithium from high magnesium/lithium ratio brine. *Adv. Funct. Mater.* **31**, 2009430 (2021).
40. F. Engelhardt, C. Maaß, D. M. Andrada, R. Herbst-Irmer, D. Stalke, Benchmarking lithium amideversusamine bonding by charge density and energy decomposition analysis arguments. *Chem. Sci.* **9**, 3111–3121 (2018).
41. M. A. Brogan, R. W. Hughes, R. I. Smith, D. H. Gregory, Structural studies of magnesium nitride fluorides by powder neutron diffraction. *J. Solid State Chem.* **185**, 213–218 (2012).
42. R.-J. Mo, S. Chen, L.-Q. Huang, X.-L. Ding, S. Rafique, X.-H. Xia, Z.-Q. Li, Regulating ion affinity and dehydration of metal-organic framework sub-nanochannels for high-precision ion separation. *Nat. Commun.* **15**, 2145 (2024).
43. T. Xu, M. A. Shehzad, D. Yu, Q. Li, B. Wu, X. Ren, L. Ge, T. Xu, Highly cation permselective metal–organic framework membranes with leaf-like morphology. *ChemSusChem* **12**, 2593–2597 (2019).
44. H. Kazemzadeh, J. Karimi-Sabet, J. T. Darian, A. Adhami, Evaluation of polymer inclusion membrane efficiency in selective separation of lithium ion from aqueous solution. *Sep. Purif. Technol.* **251**, 117298 (2020).
45. T. Xu, M. A. Shehzad, X. Wang, B. Wu, L. Ge, T. Xu, Engineering leaf-like UiO-66-$SO_3H$ membranes for selective transport of cations. *Nanomicro Lett.* **12**, 51 (2020).
46. L. Hou, W. Xian, S. Bing, Y. Song, Q. Sun, L. Zhang, S. Ma, Understanding the ion transport behavior across nanofluidic membranes in response to the charge variations. *Adv. Funct. Mater.* **31**, 2009970 (2021).
47. J. Yang, L. Li, Z. Tang, An efficient lithium extraction pathway in covalent organic framework membranes. *Matter* **4**, 2666–2668 (2021).
48. C. Zhang, Y. Mu, S. Zhao, W. Zhang, Y. Wang, Lithium extraction from synthetic brine with high $Mg^{2+}/Li^{+}$ ratio using the polymer inclusion membrane. *Desalination* **496**, 114710 (2020).
49. S. N. Kempkes, M. R. Slot, J. J. van der Broeke, P. Capiod, W. A. Benalcazar, D. Vanmaekelbergh, D. Bercioux, I. Swart, C. Morais Smith, Robust zero-energy modes in an electronic higher-order topological insulator. *Nat. Mater.* **18**, 1292–1297 (2019).
50. T. Xu, B. Wu, L. Hou, Y. Zhu, F. Sheng, Z. Zhao, Y. Dong, J. Liu, B. Ye, X. Li, L. Ge, H. Wang, T. Xu, Highly ion-permselective porous organic cage membranes with hierarchical channels. *J. Am. Chem. Soc.* **144**, 10220–10229 (2022).
51. Z. Lu, Y. Wu, L. Ding, Y. Wei, H. Wang, A Lamellar MXene ($Ti_3C_2T_x$)/PSS composite membrane for fast and selective lithium-ion separation. *Angew. Chem. Int. Ed. Engl.* **60**, 22265–22269 (2021).
52. C. E. Ren, K. B. Hatzell, M. Alhabeb, Z. Ling, K. A. Mahmoud, Y. Gogotsi, Charge- and size-selective ion sieving through $Ti_3C_2T_x$ MXene membranes. *J. Phys. Chem. Lett.* **6**, 4026–4031 (2015).
53. Q. Huang, S. Liu, Y. Guo, C. Liu, W. Jin, Separation of mono−/di-valent ions via charged interlayer channels of graphene oxide membranes. *J. Membr. Sci.* **645**, 120212 (2022).
54. Q. Wen, D. Yan, F. Liu, M. Wang, Y. Ling, P. Wang, P. Kluth, D. Schauries, C. Trautman, P. Apel, W. Guo, G. Xiao, J. Liu, J. Xue, Y. Wang, Highly selective ionic transport through subnanometer pores in polymer films. *Adv. Funct. Mater.* **26**, 5796–5803 (2016).
55. J. Abraham, K. S. Vasu, C. D. Williams, K. Gopinadhan, Y. Su, C. T. Cherian, J. Dix, E. Prestat, S. J. Haigh, I. V. Grigorieva, P. Carbone, A. K. Geim, R. R. Nair, Tunable sieving of ions using graphene oxide membranes. *Nat. Nanotechnol.* **12**, 546–550 (2017).
56. P. Wang, M. Wang, F. Liu, S. Ding, X. Wang, G. Du, J. Liu, P. Apel, P. Kluth, C. Trautmann, Y. Wang, Ultrafast ion sieving using nanoporous polymeric membranes. *Nat. Commun.* **9**, 569 (2018).
57. Y.-H. Xi, Z. Liu, J. Ji, Y. Wang, Y. Faraj, Y. Zhu, R. Xie, X.-J. Ju, W. Wang, X. Lu, L.-Y. Chu, Graphene-based membranes with uniform 2D nanochannels for precise sieving of mono−/multi-valent metal ions. *J. Membr. Sci.* **550**, 208–218 (2018).

58. T. Xu, F. Sheng, B. Wu, M. A. Shehzad, A. Yasmin, X. Wang, Y. He, L. Ge, X. Zheng, T. Xu, Ti-exchanged UiO-66-$NH_2$–containing polyamide membranes with remarkable cation permselectivity. *J. Membr. Sci.* **615**, 118608 (2020).
59. S. Hong, M. Di Vincenzo, A. Tiraferri, E. Bertozzi, R. Gorecki, B. Davaasuren, X. Li, S. P. Nunes, Precision ion separation via self-assembled channels. *Nat. Commun.* **15**, 3160 (2024).
60. Z. Zhou, K. Zhao, H.-Y. Chi, Y. Shen, S. Song, K.-J. Hsu, M. Chevalier, W. Shi, K. V. Agrawl, Electrochemical-repaired porous graphene membranes for precise ion-ion separation. *Nat. Commun.* **15**, 4006 (2024).
61. Y. Zhao, Y. Qiu, Z. Mai, E. Ortega, J. Shen, C. Gao, B. Van der Bruggen, Symmetrically recombined nanofibers in a high selectivity membrane for cation separation in high temperature and organic solvent. *J. Mater. Chem. A* **7**, 20006–20012 (2019).
62. Y. Zhao, Y. Li, J. Zhu, A. Lejarazu-Larranaga, S. Yuan, E. Ortega, J. Shen, C. Gao, B. Van der Bruggen, Thin and robust organic solvent cation exchange membranes for ion separation. *J. Mater. Chem. A* **7**, 13903–13909 (2019).
63. G. Kresse, J. Furthmuller, Efficiency of ab-initio total energy calculations for metals and semiconductors using a plane-wave basis set. *Comp. Mater. Sci.* **6**, 15–50 (1996).
64. J. P. Perdew, K. Burke, M. Ernzerhof, Generalized gradient approximation made simple. *Erratum Phys. Rev. Lett.* **78**, 1396 (1997).
65. G. Kresse, D. Joubert, From ultrasoft pseudopotentials to the projector augmented-wave method. *Phys. Rev. B* **59**, 1758–1775 (1999).
66. S. Grimme, S. Ehrlich, L. Goerigk, Effect of the damping function in dispersion corrected density functional theory. *J. Comput. Chem.* **32**, 1456–1465 (2011).



**Acknowledgments**

**Funding:** This work was supported by resources provided by the RGC General Research Fund (GRF) 2024/25 (No. 17203924) (Y. Zhao and S.Z.), the National Natural Science Foundation of China (No. 22308288) (Y. Zhao and S.Z.), and the Pawsey Supercomputing Research Centre with funding from the Australian Government and the Government of Western Australia (X. Yan and J.Z.L.). Y. Zhao and B.V.d.B. would like to acknowledge the support provided by the Fonds Wetenschappelijk Onderzoek - Vlaanderen (FWO) (Nos. 12A6823N and V461824N). L.X. would like to acknowledge the support from the Fonds Wetenschappelijk Onderzoek – Vlaanderen (FWO) (No. 12B1E24N). X. Yang would like to acknowledge the Research Foundation-Flanders (FWO) Odysseus grant (#G0F7621N) and the European Research Council (ERC) starting grant (101076550). X. Yan and J.Z.L. acknowledge grant support from the Australian Research Council (DP210103888). **Author contributions:** Conceptualization: Y. Zhao, L.X., and B.V.d.B. Methodology: Y. Zhao, X. Yan, and L.X. Investigation: Y. Zhao, L.X., and Y.Q. Visualization: Y. Zhao, X. Yan, and L.X. Supervision: Y.Z., L.X., X. Yang, and B.V.d.B. Writing—original draft: Y. Zhao, L.X., X. Yan and R.D. Writing—review and editing: All the authors. **Competing interests:** The authors declare that they have no competing interests. **Data and materials availability:** All data needed to evaluate the conclusions in the paper are present in the paper and/or the Supplementary Materials.

Submitted 1 January 2025
Accepted 11 June 2025
Published 16 July 2025
10.1126/sciadv.adv6646